electronics

MDPI

Article

Comparison between Compressive Sensing and Non-Uniform Array for a MIMO GBSAR with Elevation Resolution: Simulations and Experimental Tests

Alessandra Beni, Lapo Miccinesi and Massimiliano Pieraccini *

Department of Information Engineering, University of Florence, 50139 Firenze, Italy
* Correspondence: massimiliano.pieraccini@unifi.it

Abstract: Ground-based synthetic aperture radars (GBSAR) are popular instruments widely used for the monitoring of infrastructures. One of the main problems of ground-based interferometric radars is the elevation ambiguity. Multiple-input multiple-output (MIMO) arrays could solve this problem. This work proposes a study on possible MIMO configurations to achieve elevation resolution in ground-based radar measurements. Specifically, two array configurations are compared: a random sparse array suitable for the compressive sensing technique, and a non-uniform array. The two solutions are compared by means of simulations and experimental tests. An ad hoc system has been developed to jointly test the two configurations, and results obtained in a controlled and real urban scenario are shown. It is found that both systems are able to solve elevation ambiguity. The non-uniform array seems to achieve good performance in a general scenario, while the CS processing can outperform the other only after optimization, depending on the specific scenario and application.

Keywords: compressive sensing (CS); ground-based synthetic aperture radar (GBSAR); multiple-input multiple-output (MIMO); sparse array; radar

Citation: Beni, A.; Miccinesi, L.; Pieraccini, M. Comparison between Compressive Sensing and Non-Uniform Array for a MIMO GBSAR with Elevation Resolution: Simulations and Experimental Tests. *Electronics* **2023**, *12*, 1100. https://doi.org/10.3390/electronics12051100

Academic Editor: Yosef Pinhasi

Received: 27 January 2023
Revised: 14 February 2023
Accepted: 21 February 2023
Published: 23 February 2023

1. Introduction

Since the 2000s, ground-based synthetic aperture radar (GBSAR) systems have been proposed for the monitoring of civil infrastructures as buildings [1], bridges [2], or dams [3], and today are routinely used in civil engineering. GBSAR systems exploit the movement of the radar head on a linear (or circular) actuator in order to synthesize a large aperture in the horizontal two-dimensional plane. Thus, such systems exhibit ambiguities in the elevation direction. For the monitoring of natural scenarios, such as slopes, the missing vertical resolution does not represent a problem. On the other hand, it becomes a critical issue when architectonic structures are under test. A solution is to scan a vertical plane with the radar head. An evident drawback of this method is the measurement time, which can be very long [4].

The multiple-input multiple-output (MIMO) [5] radars are currently arousing great interest in the radar community, as they are able to drastically reduce the hardware complexity and the number of antennas while achieving performances comparable to phased array radars. The MIMO approach allows us to eliminate any mechanical system with evident advantages in terms of reliability, robustness, and cost. Different configurations have found application in ground-based radars [6–10]. Regarding the elevation ambiguity problem, in [11], the MIMO architecture is implemented on the radar head of a standard GBSAR so as to provide elevation resolution. Systems presented in [12] and [13] are examples of millimeter-wave radars, where the MIMO aperture is exploited to solve the elevation ambiguity.

In recent years, the compressive sensing (CS) technique [14–16] is gaining interest as it enables the further reduction of the number of antennas of a MIMO radar. Indeed, CS processing has been successfully applied in a wide range of fields, as it permits the reduction

of the amount of data by randomly sampling a portion. For instance, this technique proved to be efficient for the analysis of seismic data, which demands the processing of a huge amount of data, scaling with the dimension of the problem [17,18]. As for the application to MIMO radars, in [19], a CS-MIMO system is proposed for bridge monitoring. Studies have been made to optimize both the antenna array design [20,21] and the processing of the CS technique [22,23]. Authors of [24] present a theoretical comparison between the CS and sparse array processing applied to the same 4×4 MIMO radar system. Simulated results showed that the performance of CS in terms of side lobe level is better than 15 dB at the least. Additionally, non-uniform and sparse arrays have been deeply studied and ad hoc methods have been outlined to form arrays with the best performance [25–30].

It is worth noting that the fortune of MIMO radars had been particularly favored by the diffusion of millimeter-wave radars, which are small, low-cost sensors with high resolution capabilities.

In this article, the possibility of using the MIMO architecture to solve elevation ambiguity and to achieve vertical resolution is deepened. We present an experimental comparison between two different possible configurations of a MIMO radar system with 5 transmitters and 8 receivers. Specifically, we compare a random sparse array processed with the use of CS, and a non-uniform array. To this aim, ad hoc equipment capable of reproducing the virtual array configurations of both systems has been developed, starting from the prototype tested in [31]. To exhaustively compare the two configurations, single point target response has been simulated. Furthermore, measurements have been performed both in controlled and in real urban scenarios. The experimental study highlighted the slightly different performance of the two configurations. The non-uniform array proved to be more robust, suitable for different types of targets. At the same time, under specific conditions, the CS technique outperforms the other. However, this is possible only after specifically optimizing the CS processing and with a higher computational cost.

2. Materials and Methods

In this section, we briefly review the fundamentals of the compressive sensing technique applied to sparse virtual arrays. Then, we introduce the 5×8 MIMO radar system object of this study, and we explain how the two specific configurations (the sparse array for the use of CS and the non-uniform array) are arranged. In order to exhaustively compare the two configurations, both systems were simulated and results are shown.

2.1. Compressive Sensing

Compressive sensing [14,15] states that a sparse signal can be recovered by fewer samples than what is required by the Nyquist theorem. The Nyquist theorem requires that the spatial step between the array antennas has to be equal to or smaller than a quarter of wavelength ($\lambda/4$) for omnidirectional antennas. Let $\mathbf{E}$ be the vector of the N radar samples acquired by the dense array according to the Nyquist theorem. Let $\mathbf{E_{meas}}$, a subset of M samples, be the acquired radar data. Let ϕ be an M $\times$ N matrix defined as shown in Figure 1. Matrix elements are set equal to zeros in correspondence to column indices where we do not have measurements, otherwise, they are real random numbers uniformly distributed between zero and one.

Then, elements of vector $\mathbf{y}$ defined as:

$$\mathbf{y} = \phi \, \mathbf{E} \tag{1}$$

are random linear combinations of elements of the subset $\mathbf{E_{meas}}$. It is worth noting that vector $\mathbf{y}$ can be calculated from the measured data $\mathbf{E_{meas}}$.

The CS technique is based on the following strategy: to express the vector $\mathbf{y}$ in a proper basis $\{\psi\}$, on which the radar signal can be considered sparse. That is,

$$\mathbf{E} = \psi \, \mathbf{b} \, , \tag{2}$$

where **b** is the vector of coefficients in the basis $\{\psi\}$. Substituting (2) into (1), we get

$$\mathbf{y} = \theta\, \mathbf{b}\,, \tag{3}$$

with $\theta = \phi\, \psi$. Equation (3) is an ill-posed linear system with more unknown variables than equations. Nevertheless, it can be solved with the use of suitably recovery methods [31–33], with which it is possible to recover the coefficients vector **b** and hence, vector **E**. By using the CS technique, it is possible to sample radar data with a ratio $\frac{N}{M} \simeq 50\%$. For instance, in case of a 5×8 MIMO system, which corresponds to a virtual array of 40 phase centers, the CS technique can be used to reconstruct the signal acquired by a virtual array of 80 phase centers.

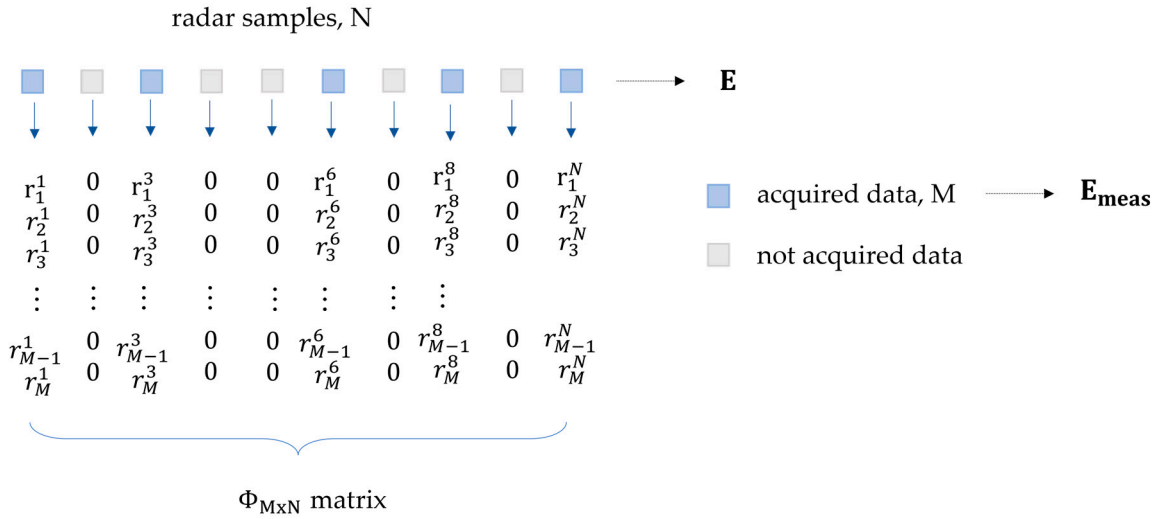

Figure 1. Theoretical scheme for the definition of the ϕ matrix. Here, the coefficients r_i^j are random numbers between zero and one, for all $i = 1, \ldots, M$ and $j = 1, \ldots, N$.

In what follows, we use the Haar wavelets basis, which proved to be particularly suitable for radar measurements in real scenarios [23], and Orthogonal Matching Pursuit (OMP) recovery method [33,34].

2.2. MIMO Configurations

For the present study, we considered a MIMO radar system with 5 transmitting (Tx) and 8 receiving (Rx) antennas working in W-band. We consider the case when the Tx antennas are located on a line and the Rx antennas on a second line are parallel to the previous one. In what follows, we work on the framework of the so-called "virtual" antenna arrays. Indeed, the signal of such a system can be equivalently studied as that being transmitted and received from the 40 phase centers (virtual antenna array) located in the plane between the Tx and Rx antennas. We performed experimental tests and simulations based on the virtual antenna array for each specific Tx, Rx configuration.

The sparse array for the use of CS was selected based on its performance characteristics. To search for possible physical configurations, we considered the antenna physical dimensions to be about 10 mm. We also imposed that the virtual array should not exceed 8 cm in length, due to physical constraints. By shifting the center of each antenna by steps of $\lambda/2$, we considered all the possible configurations by discarding patterns where two different phase centers coincide, so as to maximize the number of virtual antennas.

After these steps, we singled out about 200 possible configurations. To choose the best one for our purposes, we evaluated the peak signal-to-noise ratio (PSNR) of simulated point targets located at different positions, for each antenna pattern. The PSNR quantifies the quality of a radar signal and can be used as a method to compare radar images processed

with the use of the CS technique. The PSNR of the radar signal I_i, corresponding to the i-th pixel, can be defined as

$$\mathrm{PSNR} = 10\log_{10}\left(\frac{\max\left(|I|^2\right)}{\frac{1}{N}\sum_i |I_i - R_i|^2}\right). \tag{4}$$

where I is the radar image, N is the total number of pixels in the image, and R_i is the reference signal, on the i-th pixel, obtained with a simulated dense array, which corresponds to 80 phase centers equally spaced by $\lambda/4$.

When considering all of the possible patterns, the PSNR value is spread over 6 dB, for all the targets position. For this reason, we discarded the antennas' configuration of having low PSNR by imposing a parametric threshold. For each target's angular position φ, we evaluated the corresponding PSNR threshold as a percentage p of the maximum PNSR value reachable for the position φ. That is,

$$\mathrm{PSNR}_{\mathrm{thr}}(\varphi) = p \max_{\text{patterns}}(\mathrm{PSNR}(\varphi)). \tag{5}$$

We progressively increased the p value, so as to single out the best antenna pattern. By setting $p > 0.98$, we are left with only one configuration. The resulting real and virtual array antennas are shown in Figure 2a.

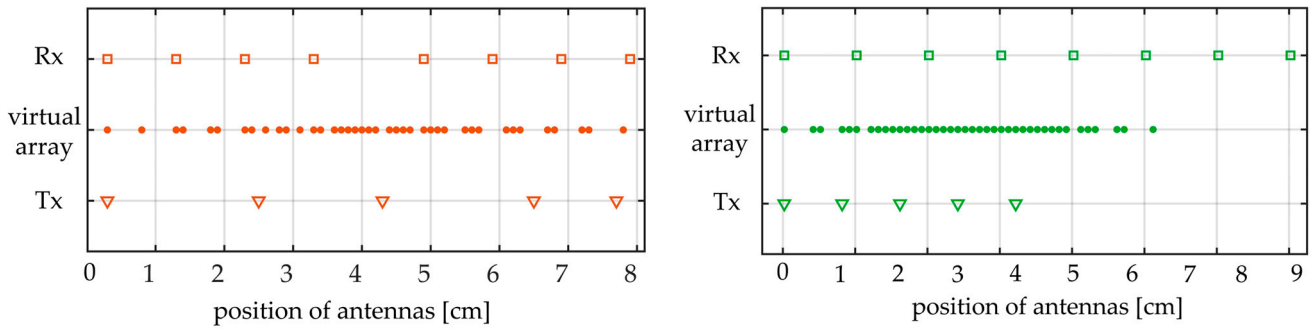

(**a**) (**b**)

Figure 2. Positions of real Tx, Rx, and virtual antenna arrays: (**a**) for the CS array; (**b**) for the non-uniform array.

Since we want to make the comparison with the same antennas, as for the non-uniform array configuration, we considered the one schematically displayed in Figure 2b. The receiving and transmitting antennas are equally spaced of different quantities, such that the resulting virtual array is symmetric and the phase centers in the central part are spaced by $\lambda/3.9$. Reasonably, holes in the virtual array do not drastically affect radar imaging, because of the windowing of edge signals. Thus, such a configuration has the advantage to form a larger aperture with respect to a dense array formed with the 40 virtual antennas of the same 5×8 MIMO.

It is worth saying that the two arrays provide different angular resolution. In fact, for GBSAR systems, the angular resolution depends on the total aperture L of the virtual linear array according to [35]

$$\Delta\theta \simeq \frac{\lambda}{2L}, \tag{6}$$

where λ is the wavelength corresponding to the central frequency of the radar signal.

2.3. Simulations

To preliminarily compare the two arrays, we simulated radar acquisitions performed with the two MIMO configurations of Figure 2. Specifically, we simulated a stepped

frequency continuous wave radar signal sweeping from 77 GHz up to 77.103 GHz, and a single point target located at different angular positions. We also simulated the acquisition with a dense array of 80 phase centers equally spaced by $\lambda/4$.

Data acquired with the sparse array of Figure 2a have been processed with the use of the CS technique, so as to reconstruct the signal of a dense array composed of 80 phase centers. As said before, we used the Haar wavelet basis and the OMP [33] recovery method, which turned out to be the most reasonable choice for most practical scenarios [23]. In what follows we will refer to this array as to the "CS array", and apply the same processing described here.

Figure 3 shows the simulation results corresponding to a target in front of the radar (Figure 3a), and to one at an angle of 1.2 rad on the left (Figure 3b). The CS array seems to achieve resolution similar to the dense array for a target located in front of the radar. On the other hand, one can notice non symmetric side lobes for the CS array, for the target of Figure 3b, while sidelobes of the non-uniform array data appear constant. From Equation (6), the nominal angular resolution values are 0.026 rad for the CS array and 0.031 rad for the non-uniform array.

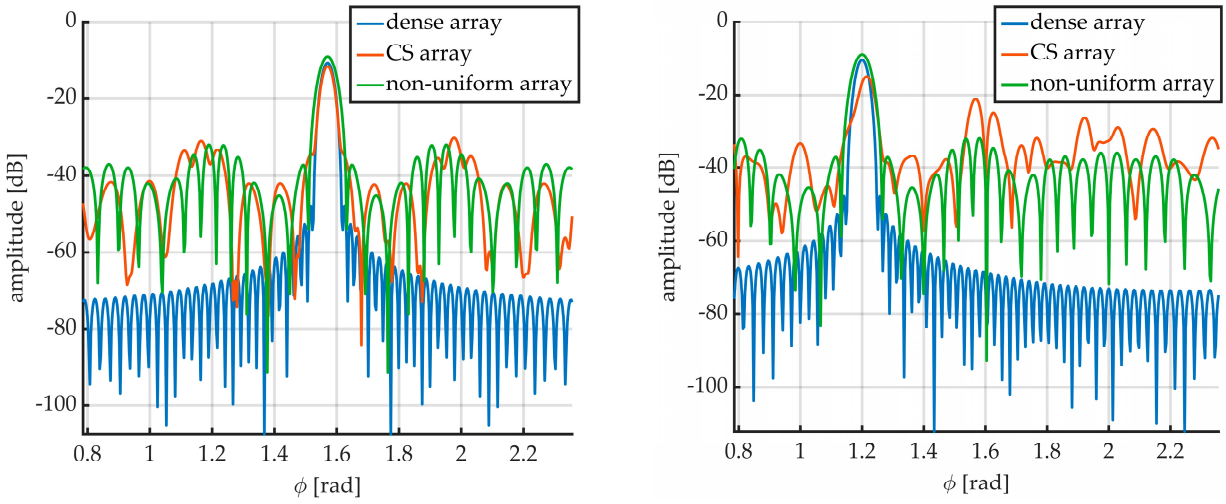

Figure 3. Simulations results of a single point target, using a dense array of 80 phase centers, the CS array shown in Figure 1a, and the non-uniform array of Figure 1b. Results in (**a**) correspond to a single point target located in front of the radar; results in (**b**) to a target located at an angle of 1.2 radians.

2.4. Radar Equipment

In order to perform measurements with the two array configurations and test their capability to solve the elevation ambiguity in ground-based radar images, we used equipment capable of reproducing the acquisitions of the virtual arrays in the vertical direction. Specifically, we used the prototype presented in [31] for 3D imaging.

A schematic of the radar system is shown in Figure 4. The radar is a commercial 3×4 MIMO by Texas Instruments. For the present application, only one Tx and one Rx antennas were used. The radar head is mounted on two linear actuators that enable the movement in two orthogonal directions. Specifically, the system continuously scans the x-axis, while moving by discrete steps of arbitrary length along the z-axis. For the present experiment, the movements along the z-axis have been tuned to replicate the antenna's position of the two virtual arrays considered. A complete scan is performed in the following way: the radar moves continuously in the horizontal direction alternatively from right to left and from left to right. Between each horizontal scan, the radar head moves by discrete steps in the vertical direction. By suitably tuning the vertical steps length, we reproduced

the antenna's position of the two virtual arrays of Figure 3 in the vertical direction. The acquisition performed is equivalent to that schematically represented in Figure 5, in case of the CS array. The vertical antenna arrays are used to acquire resolution in elevation with the use of a suitable focalization algorithm. Acquisitions performed with the CS array are processed using the CS technique before applying the focalization algorithm. In this way, it is possible to recover the measurement data which would have been acquired by a dense virtual array, with 80 phase centers equally spaced by $\lambda/4$.

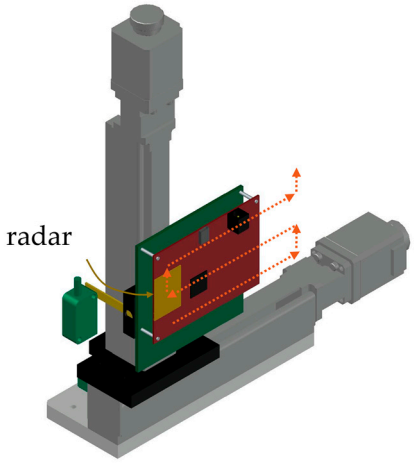

Figure 4. Scheme of the 3D GBSAR prototype used for the experiment. Orange arrows evidence the scan directions.

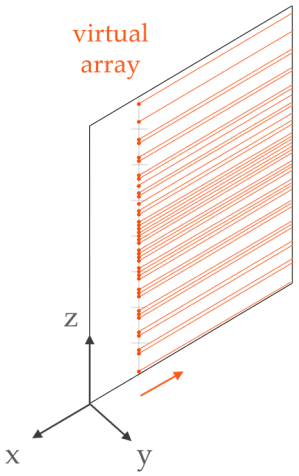

Figure 5. Scheme of the resulting scan geometry in case of the CS array in the vertical direction.

The acquired radar data were focused on a three-dimensional grid, by using a back-propagation algorithm [36]. Given the radar data sample E_{ik} corresponding to the frequency f_i, acquired by the antenna in the k-th position, the focused complex-valued radar image in a generic point (x, y, z) is obtained as,

$$I(x,y,z) = \sum_{i=1}^{N_f} \sum_{k=1}^{N_k} E_{ik} e^{j\frac{4\pi}{c} f_i R_k^{xyz}}, \quad (7)$$

where R_k^{xyz} is the distance between the k-th antenna position $\vec{R}_k$ and the point is located at coordinates (x, y, z) in the three-dimensional space. A schematic of the geometry used for calculating the distance R_k^{xyz} is shown in Figure 6. Radar images were focused on a vertical or on a horizontal plane.

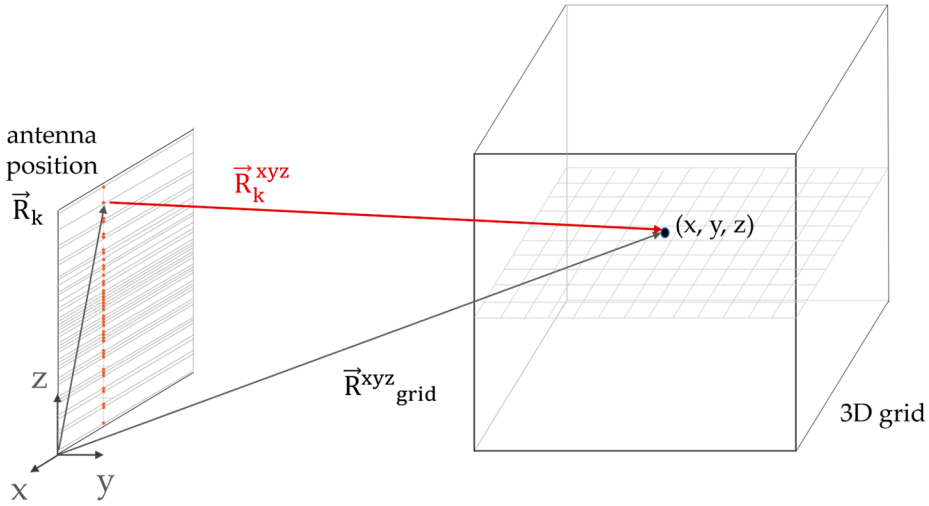

Figure 6. Geometry of the three-dimensional focalization algorithm.

3. Results

3.1. Tests in Controlled Scenario

We first performed measurements in a controlled scenario. A corner reflector with edges about 50 cm long was located in front of the radar at a distance of about 11 m, as shown in Figure 7. Figure 8 shows the resulting radar images obtained by acquisitions performed using the CS array (Figure 8a) and the non-uniform array (Figure 8b). These images are obtained by focusing the radar raw data on the y-z plane that intersects the corner reflector position. Red arrows in Figures 7 and 8 show the reference system chosen for the analysis. The white arrow points to the corner, which appears on the negative z-axis, since the radar was tilted upwards for the acquisitions. Both patterns clearly outline the corner position on the y-z plane.

Figure 7. Measurement setup for the tests in controlled scenario with a single corner reflector. As the radar is tilted up, the white arrow evidence the direction between radar and corner reflector.

The performance of the two antenna patterns is better highlighted by results displayed in Figure 9. Figure 9 shows the point spread function in the y–z plane, at a distance of 11 m, as a function of the elevation angle θ. The higher peak corresponds to the signal backscattered by the corner reflector. It is worth noting that the CS array provides a better peak resolution than the non-uniform array, despite having lower power and higher sidelobes.

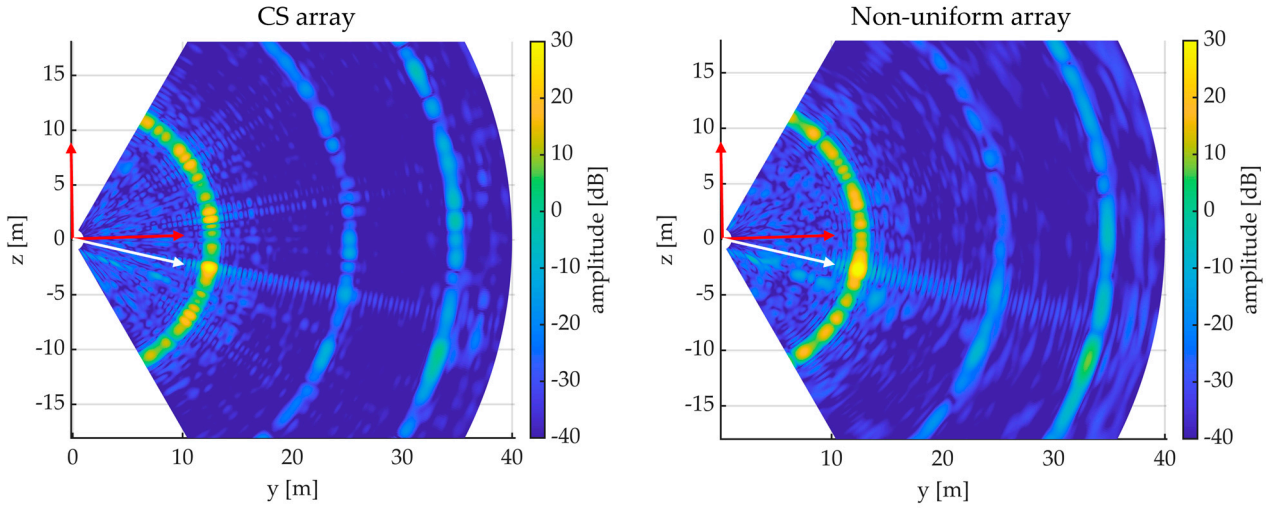

Figure 8. Radar images acquired with the CS array (**a**) and with the non-uniform array (**b**) focused on the y-z plane that intersects the corner reflector position.

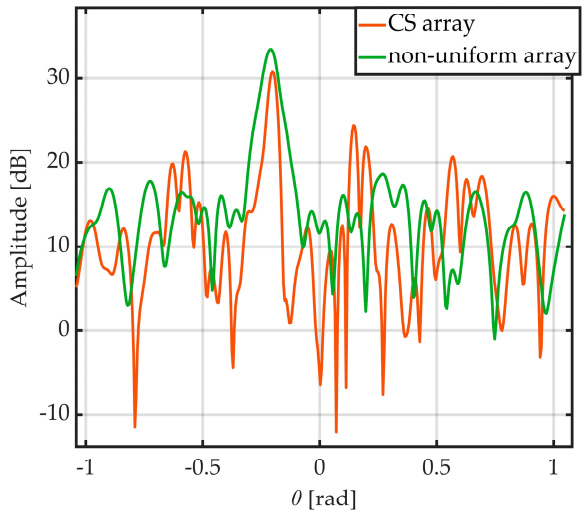

Figure 9. Results of measurements performed with the setup of Figure 7. Amplitude profile as a function of the elevation angle θ, focused on the y–z plane, at the range distance that intersects the corner reflector position.

3.2. Tests in Real Urban Scenario

The performance of the CS technique varies significantly with the target characteristics. For instance, the algorithm behaves differently on point or distributed targets [23]. In order to better assess the performance of the two configurations, we performed tests in a real urban scenario. A picture of the illuminated area is displayed in Figure 10. The radar position is outlined by the red dot, while yellow lines and circles highlight the main targets present in the area. The acquisition mode and processing were the same as for the corner reflector measurements.

Figure 10. Aerial view of the illuminated area. The radar position is highlighted by the red dot. The main targets present in the scene are highlighted in yellow. A is the upper edge of the closest building, B is the upper edge of the farthest building on the right, C is a metallic tank with industrial gas.

Figure 11 shows radar images acquired with the two modalities, focused on the x–y plane (Figure 11a,c) and on the y–z plane (Figure 11b,d), at z = 3 m above the ground and azimuth angle of 1.7 radians to the left, respectively. In each x–y (y–z) image, the dotted red lines outline the perpendicular section where the images on the y–z (x–y) plane were focused. One can notice the CS array having lower amplitude signals and higher sidelobes. Moreover, the targets shape outlined by the non-uniform array data appears clearer on the vertical y-z plane.

One of the major advantages of the CS technique is that the basis for the reconstruction of radar samples can be chosen a posteriori. Hence, we repeated the CS processing by using the fast Fourier transform (FFT) basis and the OMP reconstruction method. Results are shown in Figure 12. Although the resulting radar images appear noisier, the vertical shape of target C (see Figure 12b) is clearer than that obtained using the Haar wavelets basis (Figure 11b).

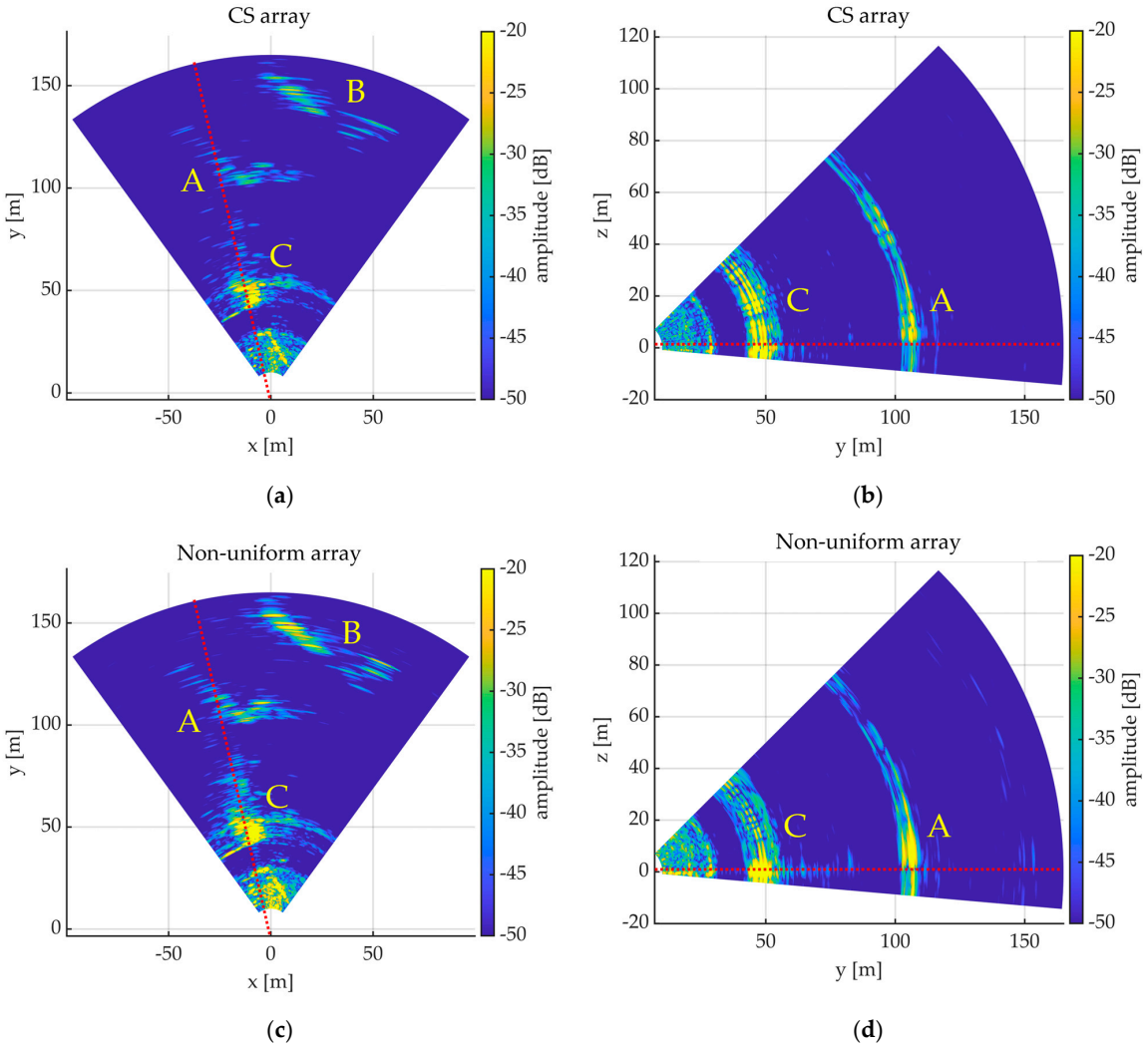

Figure 11. Radar images focused: on the x-y plane obtained with the CS array (**a**) and with the non-uniform array (**c**); on the y–z plane obtained with the CS array (**b**) and with the non-uniform array (**d**). Dotted line is the intersection between the two orthogonal image planes.

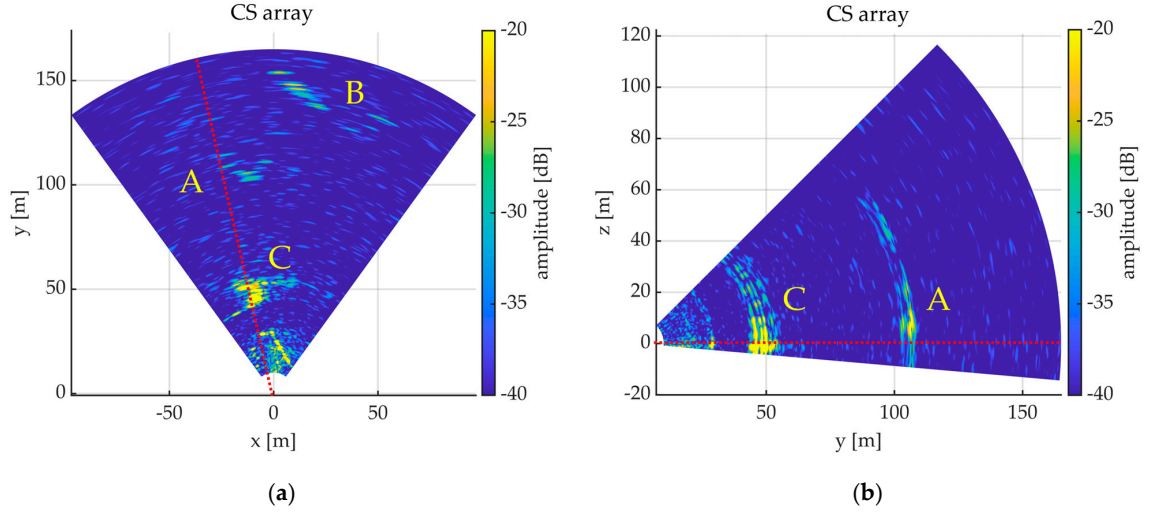

Figure 12. Radar images acquired with the CS array focused on the x-y plane (**a**) and on the y-z plane (**b**). Dotted line is the intersection between the two orthogonal image planes.

4. Discussion

In this work, we tested the performance of two possible MIMO configurations as tools for solving the elevation ambiguity of GBSAR systems. The system considered was a 5×8 MIMO. The two configurations compared were a sparse array processed with the use of the CS technique and a non-uniform array. The corresponding virtual arrays are shown in Figure 2. In the CS processing, we used the Haar wavelets basis and the OMP method for the reconstruction of the radar samples.

Simulation results reported in Figure 3 show the point target response of the two configurations. For a target located at the center of the radar field of view (see Figure 3a), the two configurations appear comparable as the sidelobe levels are almost the same. It is worth noting that the peak resolution obtained with the CS array is slightly higher and reproduces that of the dense array. However, the CS array data have non constant sidelobe levels, but rather depend on the target angle position (see Figure 3b). On the other hand, the non-uniform array configuration seems to be more robust as it results in constant and lower sidelobe levels.

Results of experimental tests performed in controlled scenario with a single corner reflector are displayed in Figures 8 and 9. In this case, the target was located approximately central, in front of the radar. One can clearly notice the higher peak resolution provided by the CS array. However, CS array data result also in a smaller signal dynamics, due to the high sidelobe levels.

Figure 11 shows radar images obtained with the two arrays in real urban scenario. Both the systems successfully imaged targets present in the area. It is worth noting that the images focused on the x-y plane (Figure 11a,c) appear similar to each other. This is because radar images on the horizontal plane are mostly influenced by the range and cross-range resolution of the system, which are the similar for both arrays, and only marginally by the elevation resolution. Therefore, the main differences are expected for images focused on the vertical y-z plane. For instance, as can be seen in Figure 11b,d, the non-uniform array image clearly outlines the height shape of the targets, while for the CS array it is more confused due to the higher sidelobes. An example is target C, highlighted by the yellow circle in Figure 10. It is a tank located at about 50 m in range from the radar, which structure is about 7 m tall. In case of the non-uniform array, we are able to distinguish the target from the sidelobes, while in case of the CS array measurement, this is not clear.

So as to further test the CS configuration, we repeated the analysis by using the FFT basis instead of the Haar wavelets for the samples reconstruction. As can be seen in Figure 12, this method leads to noisier radar images but also to a lowering of the sidelobe levels. Again, apart from the different signal to noise ratio (SNR), images focused on the x–y plane (Figures 12a and 11a,c) do not exhibit evident differences. Instead, one can notice different characteristics for images focused on the vertical plane. For instance, in Figure 12b, the lower sidelobes cause the vertical profile of target C to appear clearer than it was in Figure 11b. Thus, the FFT basis seems more suitable for imaging vertical structures such as buildings.

The results obtained showed that the non-uniform array, although with lower peak resolution, appears more robust than the CS sparse configuration since the sidelobe levels are constant as a function of the target angle. As for the CS array, the sidelobe levels are not constant, but depend on the target position. Nevertheless, the CS processing technique can be adjusted based on the specific scenario under investigation. For instance, different bases and recovery algorithms could be used in order to best fit the specific target and minimize the sidelobe levels.

5. Conclusions

In this article, a direct comparison between two MIMO configurations for the vertical resolution of a GBSAR system is presented. The study has been carried out based both on simulations and experimental tests. The MIMO configurations evaluated in this article

proved to be suitable for designing a compact and fast radar system with three-dimensional imaging capability.

Obtained results highlighted differences in the imaging performance of the two systems. The non-uniform array proved to be robust for general types of targets, although having lower peak resolution, because of the constant sidelobe levels as a function of the target angle. As for the CS array, the sidelobe levels are highly dependent on the position of the targets and can affect the measurement quality. However, the CS processing technique can be tuned according to the specific scenario, so as to minimize the sidelobes. Therefore, while the non-uniform array can be used as a standard to achieve three-dimensional resolution in general scenarios, the CS technique can be properly optimized for the specific scenario under investigation to reach higher performance.

Author Contributions: Methodology, L.M. and M.P.; software, L.M.; validation, A.B. and L.M.; formal analysis, A.B.; data curation, A.B. and L.M.; writing—original draft preparation, A.B.; writing—review and editing, A.B. and L.M.; visualization, A.B.; supervision, M.P. All authors have read and agreed to the published version of the manuscript.

Funding: This research received no external funding.

Data Availability Statement: Data are available under request.

Conflicts of Interest: The authors declare no conflict of interest.

References

1. Pieraccini, M.; Luzi, G.; Mecatti, D.; Fratini, M.; Noferini, L.; Carissimi, L.; Franchioni, G.; Atzeni, C. Remote sensing of building structural displacements using a microwave interferometer with imaging capability. *NDT E Int.* **2004**, *37*, 545–550. [CrossRef]
2. Dei, D.; Mecatti, D.; Pieraccini, M. Static Testing of a Bridge Using an Interferometric Radar: The Case Study of "Ponte degli Alpini", Belluno, Italy. *Sci. World J.* **2013**, *2013*, e504958. [CrossRef]
3. Di Pasquale, A.; Nico, G.; Pitullo, A.; Prezioso, G. Monitoring Strategies of Earth Dams by Ground-Based Radar Interferometry: How to Extract Useful Information for Seismic Risk Assessment. *Sensors* **2018**, *18*, 244. [CrossRef] [PubMed]
4. Pieraccini, M.; Rojhani, N.; Miccinesi, L. Ground Based Synthetic Aperture Radar with 3D Imaging Capability. In Proceedings of the 2018 15th European Radar Conference (EuRAD), Madrid, Spain, 26–28 September 2018; pp. 206–209. [CrossRef]
5. Fishler, E.; Haimovich, A.; Blum, R.; Chizhik, D.; Cimini, L.; Valenzuela, R. MIMO radar: An idea whose time has come. In Proceedings of the 2004 IEEE Radar Conference (IEEE Cat. No.04CH37509), Philadelphia, PA, USA, 29–29 April 2004; pp. 71–78. [CrossRef]
6. Klare, J.; Saalmann, O.; Biallawons, O. First imaging and change detection results of the MIMO radar MIRA-CLE Ka. In Proceedings of the 2013 14th International Radar Symposium (IRS), Dresden, Germany, 19–21 June 2013; Volume 1, pp. 65–70.
7. Tarchi, D.; Oliveri, F.; Sammartino, P.F. MIMO Radar and Ground-Based SAR Imaging Systems: Equivalent Approaches for Remote Sensing. *IEEE Trans. Geosci. Remote Sens.* **2013**, *51*, 425–435. [CrossRef]
8. Zeng, T.; Mao, C.; Hu, C.; Yang, X.; Tian, W. Multi-static MIMO-SAR three dimensional deformation measurement system. In Proceedings of the 2015 IEEE 5th Asia-Pacific Conference on Synthetic Aperture Radar (APSAR), Singapore, 1–4 September 2015; pp. 297–301. [CrossRef]
9. Zhao, Z.; Deng, Y.; Tian, W.; Hu, C.; Lin, Z.; Zeng, T. Dynamic Deformation Measurement of Bridge Structure Based on GB-MIMO Radar. *IEEE Trans. Geosci. Remote Sens.* **2022**, *60*, 1–14. [CrossRef]
10. Hu, C.; Wang, J.; Tian, W.; Zeng, T.; Wang, R. Design and Imaging of Ground-Based Multiple-Input Multiple-Output Synthetic Aperture Radar (MIMO SAR) with Non-Collinear Arrays. *Sensors* **2017**, *17*, 598. [CrossRef]
11. Pieraccini, M.; Miccinesi, L.; Rojhani, N. A radar with 3D imaging capability that uses synthetic aperture in azimuth and compressive sensing MIMO in elevation. In Proceedings of the 2019 16th European Radar Conference (EuRAD), Paris, France, 2–4 October 2019; pp. 65–68.
12. Miccinesi, L.; Consumi, T.; Beni, A.; Pieraccini, M. W-band MIMO GB-SAR for Bridge Testing/Monitoring. *Electronics* **2021**, *10*, 2261. [CrossRef]
13. Zhang, R.; Cao, S. Portable millimeter wave 3D imaging radar. In Proceedings of the 2017 IEEE Radar Conference (RadarConf), Seattle, WA, USA, 8–12 May 2017; pp. 0298–0303. [CrossRef]
14. Candes, E.J.; Wakin, M.B. An Introduction To Compressive Sampling. *IEEE Signal Process. Mag.* **2008**, *25*, 21–30. [CrossRef]
15. Hadi, M.A.; Alshebeili, S.; Jamil, K.; El-Samie, F.E.A. Compressive sensing applied to radar systems: An overview. *SIViP* **2015**, *9*, 25–39. [CrossRef]
16. Rossi, M.; Haimovich, A.M.; Eldar, Y.C. Spatial Compressive Sensing for MIMO Radar. *IEEE Trans. Signal Process.* **2014**, *62*, 419–430. [CrossRef]

17. Herrmann, F.J.; Friedlander, M.P.; Yilmaz, O. Fighting the Curse of Dimensionality: Compressive Sensing in Exploration Seismology. *IEEE Signal Process. Mag.* **2012**, *29*, 88–100. [CrossRef]
18. Mosher, C.; Li, C.; Morley, L.; Ji, Y.; Janiszewski, F.; Olson, R.; Brewer, J. Increasing the efficiency of seismic data acquisition via compressive sensing. *Lead. Edge* **2014**, *33*, 386–391. [CrossRef]
19. Pieraccini, M.; Miccinesi, L. An Interferometric MIMO Radar for Bridge Monitoring. *IEEE Geosci. Remote Sens. Lett.* **2019**, *16*, 1383–1387. [CrossRef]
20. Rojhani, N.; Passafiume, M.; Lucarelli, M.; Collodi, G.; Cidronali, A. Assessment of Compressive Sensing 2 × 2 MIMO Antenna Design for Millimeter-Wave Radar Image Enhancement. *Electronics* **2020**, *9*, 624. [CrossRef]
21. Ajorloo, A.; Amini, A.; Tohidi, E.; Bastani, M.H.; Leus, G. Antenna Placement in a Compressive Sensing-Based Colocated MIMO Radar. *IEEE Trans. Aerosp. Electron. Syst.* **2020**, *56*, 4606–4614. [CrossRef]
22. Feng, W.; Friedt, J.-M.; Nico, G.; Sato, M. 3-D Ground-Based Imaging Radar Based on C-Band Cross-MIMO Array and Tensor Compressive Sensing. *IEEE Geosci. Remote Sens. Lett.* **2019**, *16*, 1585–1589. [CrossRef]
23. Pieraccini, M.; Rojhani, N.; Miccinesi, L. Compressive Sensing for Ground Based Synthetic Aperture Radar. *Remote Sens.* **2018**, *10*, 1960. [CrossRef]
24. Pieraccini, M.; Miccinesi, L.; Boni, E. Comparison between Sparse Array and Compressive Sensing for designing a 4 × 4 MIMO radar. In Proceedings of the 2020 IEEE Radar Conference (RadarConf20), Florence, Italy, 21–25 September 2020; pp. 1–4. [CrossRef]
25. Michelini, A.; Coppi, F.; Bicci, A.; Alli, G. SPARX, a MIMO Array for Ground-Based Radar Interferometry. *Sensors* **2019**, *19*, 252. [CrossRef]
26. Syeda, R.Z.; Savelyev, T.G.; van Beurden, M.C.; Smolders, A.B. Sparse MIMO Array for Improved 3D mm- Wave Imaging Radar. In Proceedings of the 2020 17th European Radar Conference (EuRAD), Utrecht, The Netherlands, 10–15 January 2021; pp. 342–345. [CrossRef]
27. Gumbmann, F.; Schmidt, L.-P. Millimeter-Wave Imaging With Optimized Sparse Periodic Array for Short-Range Applications. *IEEE Trans. Geosci. Remote Sens.* **2011**, *49*, 3629–3638. [CrossRef]
28. Zhuge, X.; Yarovoy, A.G. Study on Two-Dimensional Sparse MIMO UWB Arrays for High Resolution Near-Field Imaging. *IEEE Trans. Antennas Propag.* **2012**, *60*, 4173–4182. [CrossRef]
29. Mateos-Núñez, D.; González-Huici, M.A.; Simoni, R.; Khalid, F.B.; Eschbaumer, M.; Roger, A. Sparse array design for Automotive MIMO Radar. In Proceedings of the 2019 16th European Radar Conference (EuRAD), Paris, France, 2–4 October 2019; pp. 249–252.
30. Schmid, C.M.; Feger, R.; Wagner, C.; Stelzer, A. Design of a linear non-uniform antenna array for a 77-GHz MIMO FMCW radar. In Proceedings of the 2009 IEEE MTT-S International Microwave Workshop on Wireless Sensing, Local Positioning, and RFID, Cavtat, Croatia, 24–25 September 2009; pp. 1–4. [CrossRef]
31. Beni, A.; Consumi, T.; Miccinesi, L.; Pieraccini, M. W-Band GB-SAR for 3D Imaging. In Proceedings of the 2022 19th European Radar Conference (EuRAD), Milan, Italy, 28–30 September 2022; pp. 61–64. [CrossRef]
32. Yang, A.Y.; Sastry, S.S.; Ganesh, A.; Ma, Y. Fast ℓ1-minimization algorithms and an application in robust face recognition: A review. In Proceedings of the 2010 IEEE International Conference on Image Processing, Hong Kong, China, 26–29 September 2010; pp. 1849–1852. [CrossRef]
33. Tropp, J.A.; Gilbert, A.C. Signal Recovery From Random Measurements Via Orthogonal Matching Pursuit. *IEEE Trans. Inf. Theory* **2007**, *53*, 4655–4666. [CrossRef]
34. Baraniuk, R.G. Compressive Sensing [Lecture Notes]. *IEEE Signal Process. Mag.* **2007**, *24*, 118–121. [CrossRef]
35. Hong, W.; Zhang, Y.; Lin, Y.; Li, Y.; Bai, Z.; Zhang, Q.; Lv, S.; Liu, H.; Song, Y. Ground-Based Differential Interferometry SAR: A Review. *IEEE Geosci. Remote Sens. Mag.* **2020**, *8*, 43–70. [CrossRef]
36. Pieraccini, M.; Miccinesi, L. ArcSAR: Theory, Simulations, and Experimental Verification. *IEEE Trans. Microw. Theory Tech.* **2017**, *65*, 293–301. [CrossRef]